Uniform small metal nanoparticles anchored on CeO_2 nanorods driven by electroless chemical deposition

Zheng Chen, Fang-Xian Cao, Wei Gao, Qing-Chen Dong , **Yong-Quan Qu***

Abstract We report a facile electroless chemical deposition (ECD) method to deposit uniform Pd nanoparticles ((2.5 ± 0.6) nm) on CeO_2 nanorods (PdNPs/CeO_2-ECD) through the interface redox reaction between the reduced CeO_2 and Na_2PdCl_4. PdNPs/CeO_2-ECD exhibits a stronger electronic metal–support interaction (EMSI) evidenced by higher reducibility and stronger anti-sintering capability at high temperatures, compared to that prepared by the conventional impregnation method. Such an EMSI effect of PdNPs/CeO_2-ECD significantly improves its catalytic activity in CO oxidation. Besides, the chlorine residue-free catalysts through ECD process avoid the deleterious effect of chlorine on CO oxidation. This ECD process can further be extended to deposit various uniform nanoscaled noble metals (Au, Ag, Pt, Ru, Rh, etc.) on CeO_2, which may deliver their potentials in advanced catalysis.

Keywords Electroless chemical deposition; Electronic metal–support interaction; Pd/CeO_2; CO oxidation

Zheng Chen and Fang-Xian Cao have contributed equally to this work.

Z. Chen, Q.-C. Dong, Y.-Q. Qu
MOE Key Laboratory of Interface Science and Engineering in Advanced Materials and Research Center of Advanced Materials Science and Technology, Taiyuan University of Technology, Taiyuan 030024, China

F.-X. Cao, W. Gao, Y.-Q. Qu*
Center for Applied Chemical Research, Frontier Institute of Science and Technology, Xi'an Jiaotong University, Xi'an 710049, China
e-mail: yongquan@mail.xjtu.edu.cn

1 Introduction

Heterogeneous catalysts integrating catalytically active components on various supports have attracted considerable efforts and shown their potential applications in energy conversion, environmental remediation and green catalysis [1–3]. Generally, the catalytic performance of heterogeneous catalysts is determined by active species (e.g., noble metals, transition metals) as well as supports (e.g., zeolite, metal oxides). The synergistic interactions between active centers and supports can significantly enhance the catalytic activity and selectivity, preserve the dispersion of active species on supports and improve the catalytic stability under the reaction environments [4]. Noble metals (Pt, Pd, Au, Ru, Rh, etc.) anchored on CeO_2 show a strong electronic metal–support interaction (EMSI), which can improve their thermal stability and catalytic activity effectively [5–10]. Many factors including the surface physicochemical property of supports, morphology and size of active species, post-treatments and synthetic techniques play important roles in regulating the EMSI effects of heterogeneous catalysts [11–15].

Various synthetic techniques including impregnation (IM), deposition–precipitation (DP) and co-precipitation have generally been employed to prepare the rationally designed catalysts for desired catalysis [13]. However, the usage of complex chemical systems may introduce residues in catalysts, which may be poisonous to catalysis [16]. Some techniques such as atomic layer deposition (ALD) have also been developed to deposit uniform metal catalysts on supports with a prominent EMSI effect. However, the expensive instruments with high energy consumption and low synthetic productivity cannot satisfy the practical applications in a large scale. Compared with those

conventional approaches and recently developed synthesis strategies, the electroless chemical deposition (ECD) method, in situ deposition of metal catalysts on various substrates, is of much competitiveness due to the advantages of low-cost, surfactant-free, low-energy consumption and scalable synthesis. ECD process is a non-galvanic process, which involves the simultaneous reactions in the liquid solution without the use of external electrical power. Such a deposition is driven by the redox potential difference of two half-reactions to overcome the inherent energy barriers in the solution environments. Successful ECD planting of metal nanoparticles on surfaces of various supports such as $WO_{2.72}$, $Ce(OH)_3$ and titanium(III) oxides has been realized [16–21].

In case of $Ce(OH)_3$, synthesis of supports and ECD process has to be performed in oxygen-free environment due to the easy oxidation of Ce^{3+} species. Herein, we report a more facile ECD method to in situ deposit uniform and small Pd nanoparticles (PdNPs, $\sim$ 2.5 nm) on CeO_2 nanorods (PdNPs/CeO_2-ECD) under ambient conditions. Synthesis of catalysts involves the chemical reduction of CeO_2 nanorods by ascorbic acid (AA) and subsequent ECD deposition of Pd species on CeO_2 driven by the interface redox reaction between the reduced CeO_2 and Na_2PdCl_4. Compared to PdNPs on CeO_2 nanorods prepared by impregnation (PdNPs/CeO_2-IM), PdNPs/CeO_2-ECD avoids the chlorine contamination and exhibits more pronounced EMSI effect, as evidenced by its higher reducibility, surface electron enrichment and stronger anti-sintering capability at high temperatures. All features of PdNPs/CeO_2-ECD delivered its high catalytic activity of CO oxidation. Besides, this ECD process can be universal to deposit other noble metal catalysts (Ag, Au, Pt, Ru, Rh, etc.) on CeO_2 as heterogeneous catalysts.

2 Experimental

2.1 Synthesis of CeO_2 nanorods

CeO_2 nanorods were synthesized via a hydrothermal method modified from the previous studies [22, 23]. Briefly, 5 ml $Ce(NO_3)_3$ aqueous solution (0.8 mol·L^{-1}) was added to 75 ml NaOH aqueous solution (6.4 mol·L^{-1}) and stirred for 30 min. Then, the mixture was transferred to a 100-ml Teflon-lined autoclave and kept at 100 °C for 24 h. The obtained precipitates were washed by distilled water and ethanol alternatively three times and dried at 60 °C overnight.

2.2 ECD process for metal nanoparticles planting on CeO_2 nanorods

The ECD method was performed through a two-step reaction. For PdNPs/CeO_2-ECD samples, typically, 100 mg CeO_2 nanorods was dispersed in 50 ml distilled water, followed by the addition of 1.0 ml 0.1 mol·L^{-1} ascorbic acid under stirring. After 30 min, the reduced CeO_2 nanorods were centrifuged off and washed with copious amounts of distilled water three times and then re-dispersed in distilled water by ultrasonic with a concentration of 1.0 mg·ml^{-1}. Next, the desired amount of Na_2PdCl_4 solution was added into 100 ml stock reduced CeO_2 nanorods solution under stirring for ECD process with reaction time of tens of minutes. For other noble metal nanoparticles, $RuCl_3$, $RhCl_3$, $AgNO_3$, Na_2PtCl_6 and $HAuCl_4$ were used as metal precursors for the ECD process, respectively.

For synthesis of 2.0 wt% PdNPs/CeO_2 samples, two approaches of the one-shot and multiple-cycle ECD processes were employed. For one-shot reaction, the desired amount of Na_2PdCl_4 solution was directly added into the aqueous dispersion of the reduced CeO_2 nanorods to achieve the theoretical Pd loading of 2.0 wt%. For the multiple-cycle ECD process, the ECD process for the 0.5 wt% PdNPs/CeO_2 catalysts was repeated four times consecutively.

2.3 Synthesis of PdNPs/CeO_2 by impregnation method

Briefly, 100 mg CeO_2 nanorods was suspended in 5 ml ethanol solution with desired amount of Na_2PdCl_4 at room temperature for 1 h. Later, the mixture was heated to 100 °C until the solution volatilized completely. Finally, the PdNPs/CeO_2-IM catalysts were obtained after reduction by a mixed gas of 5 vol% H_2/Ar at 350 °C for 60 min.

2.4 Characterization

Transmission electron microscopy (TEM) measurements were taken using a Hitachi HT-7700 electron microscope with an accelerating voltage of 120 kV. High-resolution TEM (HRTEM) images were obtained on the FEI Tecnai G2 F20 S-TWIN microscope with the accelerating voltage of 200 kV. X-ray diffraction (XRD) patterns were taken using a Rigaku Powder X-ray diffractometer with Cu Kα radiation. Inductively coupled plasma atomic emission spectroscopy (ICP-AES) measurements for analysis of elemental contents were taken using an Agilent 7500ce instrument. X-ray photoelectron spectra (XPS) were acquired on a Thermo Electron Model K-Alpha with Al Kα as the excitation sources. Raman spectra were recorded on

a Renishaw inVia Reflex laser microprobe Raman spectroscopy with the excitation wavelength of 514 nm.

2.5 H_2 temperature-programmed reduction (H_2-TPR) measurements

H_2-TPR was carried out in a ChemBET TPR/TPD3000 apparatus. For a typical measurement, 20 mg unreduced sample was loaded into the reactor. Prior to measurement, the samples were pre-treated in Ar at 200 °C for 1 h and cooled down to room temperature. Then, a mixture gas of 5 vol% H_2/Ar (30 ml·min^{-1}) was introduced at room temperature under a temperature-programmed procedure with a ramping rate of 10 °C·min^{-1}.

2.6 Pd dispersion of catalysts

CO chemisorption was performed on a quantachrome instrument (ChemBET TPR/TPD chemisorption analyzer), which was employed to determine the Pd dispersions of various Pd/CeO_2 catalysts. A given amount of 10 vol% CO in He (50 μl) was introduced in a pulse per 5 min at room temperature until the intensity of the peak reached a constant value. Before test, all samples were calcined at 350, 425 and 500 °C in air for 4 h, respectively.

2.7 Catalytic CO oxidation

CO oxidation reaction was used as a probe reaction to compare the catalytic activity of the PdNPs/CeO_2 catalysts prepared via different methods. Before the reaction, all catalysts were treated under a 50 ml·min^{-1} flowing mixture gas of H_2/Ar with the volumetric ratio of 1:9 at 350 °C for 60 min. For the CO oxidation reaction, the activity of catalysts was evaluated on a homemade fixed-bed quartz reactor connected to a flow apparatus with the mass flow controllers. The mixture gas of 0.5 ml·min^{-1} CO, 0.5 ml·min^{-1} O_2 and 49 ml·min^{-1} Ar was delivered into the reactor where 250 mg pre-treated catalysts (150–280 μm) was filled. The temperature ramping rate was controlled at 5 °C·min^{-1}. The progress of CO oxidation was monitored by an online gas chromatograph equipped with a flame ionization detector (FID).

3 Results and discussion

3.1 TEM and XRD results

CeO_2 nanorods were synthesized according to a previously reported hydrothermal method [22, 23]. CeO_2 nanorods exhibited a smooth surface with a length of 100–200 nm and a diameter of $\sim$ 10 nm (Fig. S1). AA, a harmless natural product, was employed to reduce CeO_2 nanorods. The reduced CeO_2 nanorods preserved their rodlike morphological features as that of the freshly synthesized nanorods (Fig. 1a). Derived from XPS spectra of the Ce 3d core level (Fig. S2 and Fig. 2a), the surface Ce^{3+} content of the reduced CeO_2 nanorods was increased from 17.3 at% of as-synthesized CeO_2 nanorods to 31.6 at%, indicating the successful reduction of CeO_2 nanorods. After the ECD process between the reduced CeO_2 and the aqueous Na_2PdCl_4 precursor, the typical TEM image (Fig. 1b) shows the similar rodlike morphology decorated with uniform and small nanoparticles of (2.5 ± 0.6) nm (Fig. S3). The fringe spacing (0.282 nm) of the deposited nanoparticles in the HRTEM corresponds to the (200) facet of PdO_x, demonstrating the formation of Pd species on the surface of the CeO_2 nanorods (Fig. 1c). The results of XPS can further confirm that most of the Pd species exist in + 2 valence state (Fig. S4). The formation of PdO_x may be attributed to the ECD and subsequent oxidation of the metallic Pd by the dissolved oxygen. To confirm this hypothesis, the ECD process was also performed in the degassed conditions under the protection of high-purity Ar (99.999%), where Pd precursor (Na_2PdCl_4) and the reduced CeO_2 nanorods were used. The obtained nanoparticles on CeO_2 were identified as Pd metal, with a fringe spacing of 0.195 nm corresponding to the (200) facet of Pd (Fig. S5). Thus, the oxidation of metal nanoparticles might be avoidable in the absence of oxygen. XRD patterns in Fig. 1g show that the as-synthesized CeO_2 nanorods, reduced CeO_2 nanorods and PdNPs/CeO_2-ECD are cubic fluorite structures (PDF No. 75-0076). Thus, the post-treatment of chemical reduction and ECD process did not induce the morphology and the phase change of CeO_2 nanorods. The actual Pd loadings on supports were determined by ICP-AES. For the PdNPs/CeO_2-ECD catalysts with a theoretical Pd loading of 0.5 wt%, ICP-AES result (Fig. 1f) reveals that Pd was successfully and completely planted. Notably, it only took tens of minutes for the Pd planting, indicating the efficient and time-saving process of ECD technique.

To control the planting amount of Pd on CeO_2 is also expected for the ECD technique. Specifically, for a theoretical Pd loading of 2 wt%, both large nanoparticles (> 5.0 nm) and small nanoparticles ($\sim$ 2.5 nm) were co-deposited on CeO_2 nanorods when the desired Pd source was directly added through a one-shot injection (Fig. 1e). To solve this problem, the strategy by repeating the ECD process with a low Pd loading was found to obtain uniform and small PdO_x nanoparticles. As shown in Fig. 1d, performing the ECD process for four cycles with a 0.5 wt% Pd loading for each cycle led to the formation of PdO_x nanoparticles with a uniform size of (2.8 ± 0.8) nm (Fig. S6), which was very close to that of 0.5 wt% PdNPs/
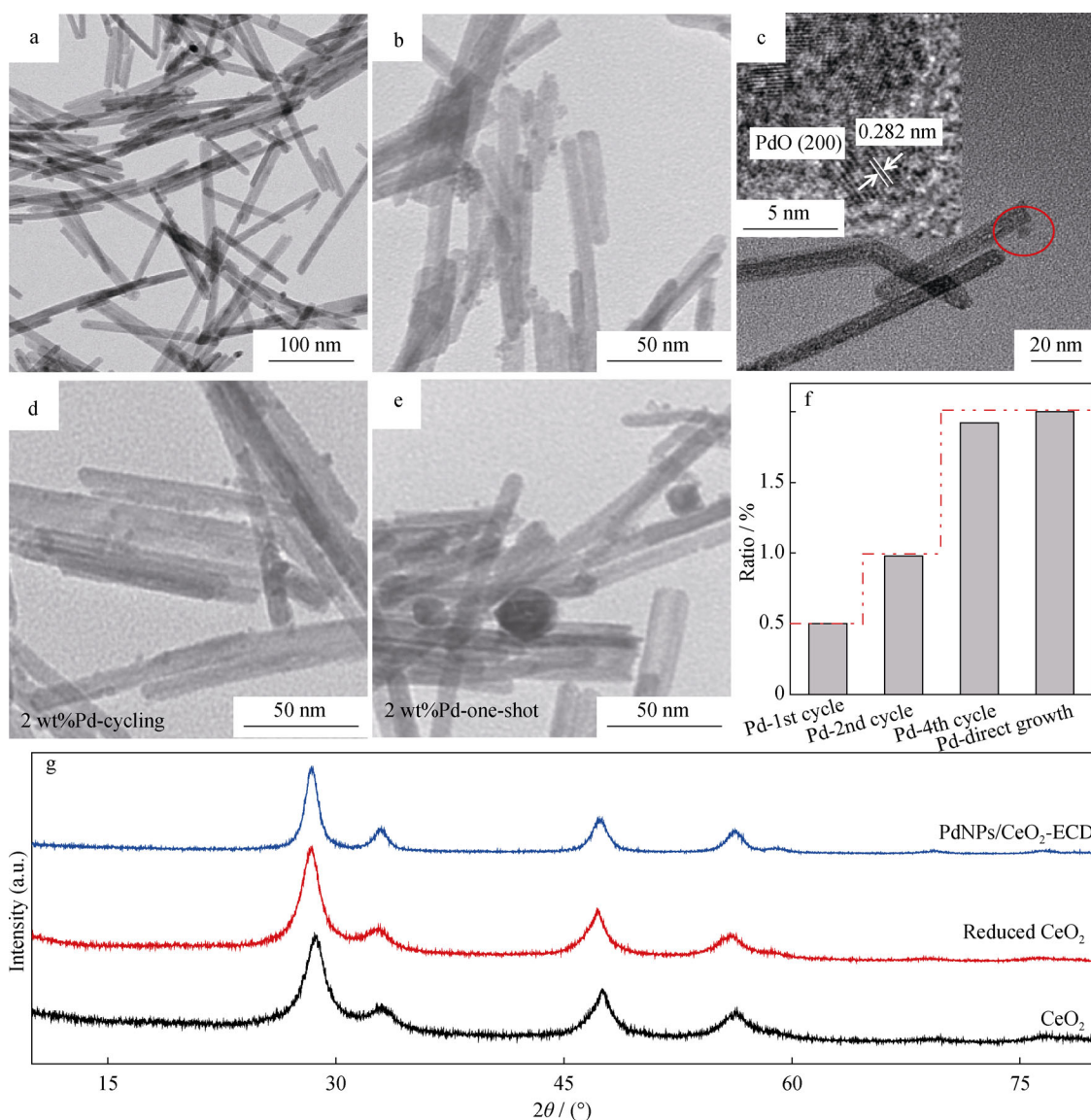
Fig. 1 Typical TEM images of **a** reduced CeO$_2$ nanorods and **b** 0.5 wt% PdNPs/CeO$_2$ prepared by ECD method; **c** HRTEM image of metal nanoparticles on 0.5 wt% PdNPs/CeO$_2$ prepared by ECD method; TEM images of **d** 2 wt% PdNPs/CeO$_2$ prepared by adding Pd sources over four ECD cycling reactions and **e** 2 wt% PdNPs/CeO$_2$ prepared by adding Pd sources over a one-shot reaction; **f** ICP-AES results of Pd loadings via one-shot ECD process and multiple-cycle ECD process; **g** XRD patterns of as-synthesized CeO$_2$ nanorods, reduced CeO$_2$ nanorods and PdNPs/CeO$_2$-ECD

CeO$_2$ ((2.5 $\pm$ 0.6) nm, Fig. 1b). The actual Pd loading amount of catalysts prepared through the repeated ECD process was close to the theoretical value (Fig. 1f). The above results exhibit that the cycling of the ECD process preserves the uniform and small nanoparticles, when the high loading of metal is expected. The completely different growth behaviors of one-shot and multiple-cycle methods can be attributed to the preferential nucleation at the surface defects of CeO$_2$ nanorods. For one-shot synthesis, some of the formed PdO$_x$ nanoparticles might serve as the nuclei for the ripening growth of larger particles, when more metal precursors were available. Consequently, the

uneven size distribution of PdO$_x$ nanoparticles was observed (Fig. 1e). In contrast, the multiple-cycle synthesis creates the freshly exposed surface defects of CeO$_2$ nanorods after each chemical reduction, which are preferential sites for the nucleation and growth of Pd species in the presence of limited amount of metal precursor. Thus, it results in the formation of uniform and small PdO$_x$ nanoparticles. Moreover, as shown in the scalable optical and TEM images (Fig. S7), 1.0 g PdNPs/CeO$_2$ nanorods (Pd based, 0.5 wt%) was synthesized through a one-shot ECD reaction, with similar size of Pd nanoparticles ($\sim$ 2.6 nm).
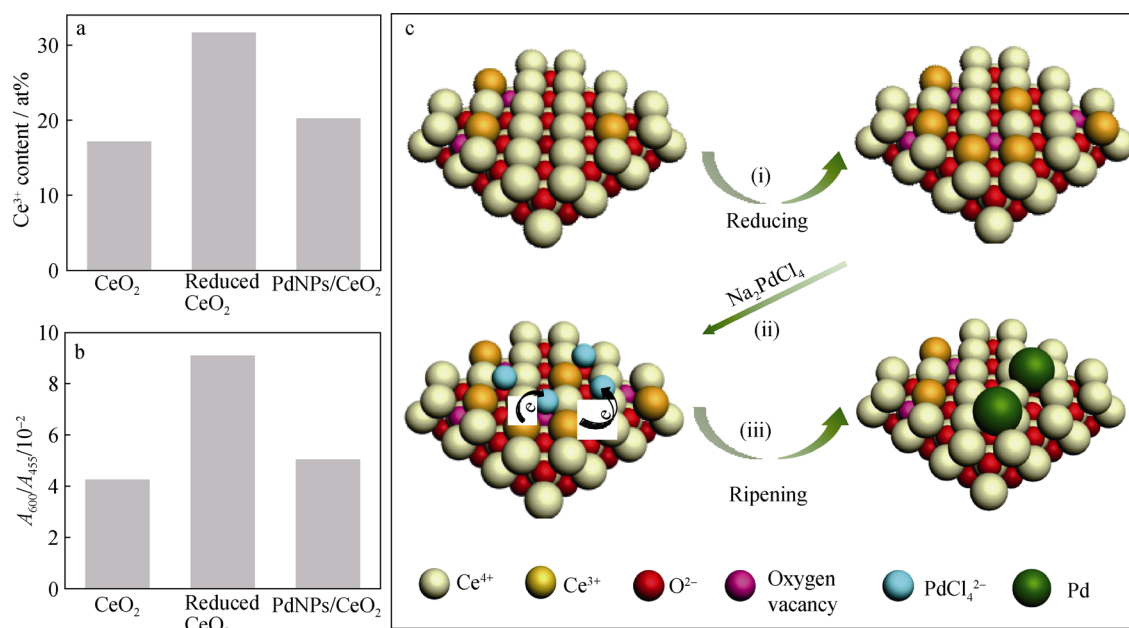
Fig. 2 Evolutions in **a** surface Ce^{3+} content derived from XPS Ce 3d core levels and **b** relative concentrations of oxygen vacancy derived from Raman spectra for as-synthesized CeO_2, reduced CeO_2 and obtained PdNPs/CeO_2 prepared by ECD method; **c** schematic diagram of ECD reacting mechanism based on three steps: (i) chemical reduction of CeO_2, (ii) nucleation of Pd nanoparticles on CeO_2 nanorods with electron transfer and (iii) ripening of Pd particles

3.2 Proposed synthetic mechanism

To identify the role of Ce^{3+} species for ECD process, the XPS technique was used to examine the surface Ce^{3+} species. The surface Ce^{3+} content delivered the initial increase from 17.3 at% of the as-synthesized CeO_2 nanorods to 31.6 at% of the reduced CeO_2 nanorods and the subsequent decrease to 18.1 at% after ECD process (Fig. 2a and Fig. S2). The results indicate that Ce^{3+} species serve as the reducing regent by donating electrons to metal precursor [18]. The evolution of oxygen vacancy accompanied with changes in Ce^{3+} content was also monitored by Raman spectroscopy. The Raman peaks at $\sim$ 455 and $600\ cm^{-1}$ in Raman spectra (Fig. S8) are ascribed to the vibrational mode (F_{2g}) of the fluorite-type structure and the oxygen vacancies of CeO_2, respectively [23]. The ratio of integral areas of peaks at 600 and $455\ cm^{-1}$ (A_{600}/A_{455}) is used as an indicator to reflect the concentration of oxygen vacancy. As shown in Fig. 2b and Fig. S8, the ratios of A_{600}/A_{455} are increased from 0.0424 of as-synthesized CeO_2 to 0.0908 of the reduced CeO_2 nanorods and decreased again to 0.0503 after planting of PdO_x nanoparticles. The recovery of the concentration of oxygen vacancy demonstrates that the formation of PdO_x nanoparticles consumes the surface Ce^{3+} species during the ECD process. Therefore, the ECD process for planting PdNPs on CeO_2 is illustrated in Fig. 2c, in which the electron transfers from the reduced CeO_2 with a high surface Ce^{3+} content and large concentration of oxygen

vacancy to metal precursors boosts the nucleation and ripening of PdO_x.

3.3 H_2-TPR and anti-sintering capability

Aiming at demonstrating the metal/support interaction and surface reducibility, temperature-programmed reduction by hydrogen (H_2-TPR) was performed. As comparative studies, the conventional impregnation method was also used to deposit PdNPs on CeO_2 nanorods ($\sim$ 2.4 nm), named as PdNPs/CeO_2-IM (Fig. S9). The Pd loading was fixed at 0.5 wt% for all catalysts. In their H_2-TPR profiles (Fig. 3a), one peak centered at $\sim$ 127 °C was observed for the PdNPs/CeO_2-ECD catalysts which was related to the reduction of the PdO_x species and part of support surface oxygen species strongly interacted with PdO_x [24]. However, two overlapping reduction peaks at 200–280 °C appeared on the H_2-TPR profile of the PdNPs/CeO_2-IM catalysts, corresponding to the reduction of PdO_x and interfacial oxygen species due to spillover effect. The reduction peak for PdNPs/CeO_2-ECD shifts to lower temperature, indicating an easier reduction of surface oxygen species. Moreover, the higher reducibility of surface oxygen species of the PdNPs/CeO_2-ECD catalysts indicates that a stronger interaction between Pd nanoparticles and supports is induced by ECD process, compared with that of the PdNPs/CeO_2-IM catalysts [25–27].

To further evaluate the EMSI effects between Pd nanoparticles and CeO_2 supports, the anti-sintering
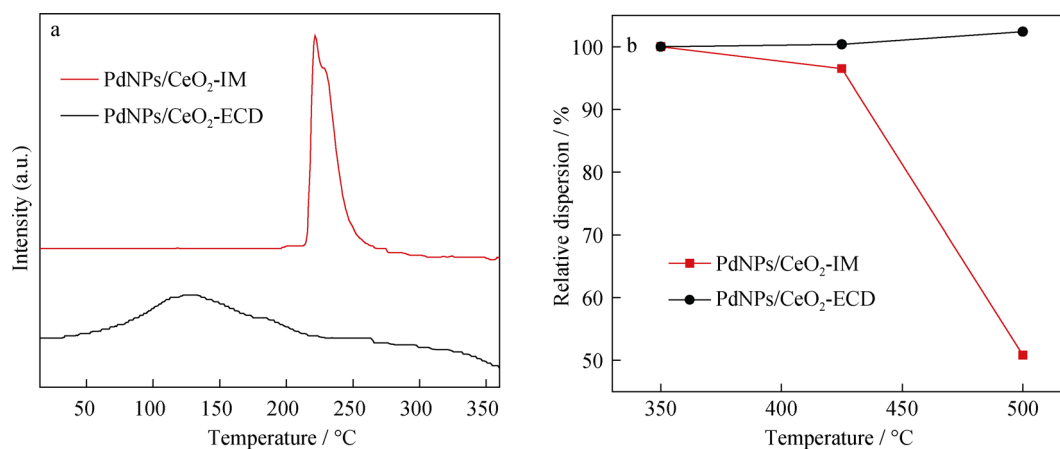
Fig. 3 H₂-TPR and anti-sintering capability to describe EMSI effects of PdNPs/CeO₂-ECD and PdNPs/CeO₂-IM catalysts characterized by **a** H₂-TPR and **b** CO dispersions after thermal treatments at 350, 425 and 500 °C
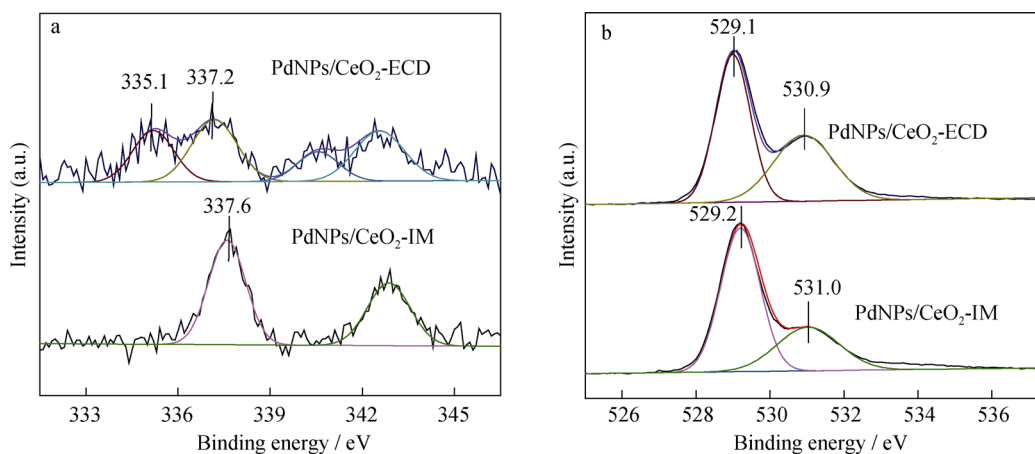

Fig. 4 a Pd 3d and **b** O 1s XPS spectra of PdNPs/CeO₂-ECD and PdNPs/CeO₂-IM

capability of PdNPs/CeO₂-ECD and PdNPs/CeO₂-IM was tested under high temperatures. The Pd dispersions measured by CO chemisorption after thermal treatments under various temperatures (350, 425 and 500 °C) are shown in Fig. 3b and Table S1. The Pd dispersions of the PdNPs/CeO₂-ECD catalysts remained near the same values (around 25.5%, Table S1) with the increase in the calcination temperatures. In contrast, the Pd dispersions of PdNPs/CeO₂-IM significantly dropped from 37.6% at 350 °C to 36.3% at 425 °C and 19.1% at 500 °C (Table S1). It can be attributed to the thermal sintering of Pd nanoparticles due to the weaker interaction between Pd and CeO₂ support.

3.4 XPS analysis

Oxidation states of Pd species and surface oxygen species of catalysts were further analyzed. As shown in Fig. 4a, the PdNPs/CeO₂-ECD catalysts show two Pd 3d$_{5/2}$ peaks at

335.1 and 337.2 eV, which can be attributed to the typical characteristics of metallic Pd and Pd^{2+}, respectively, while the PdNPs/CeO₂-IM catalysts only exhibit one oxidized Pd 3d$_{5/2}$ peak at 337.9 eV, which shifts to higher binding energy compared to the oxidized peak of PdNPs/CeO₂-ECD. The results reveal that the PdNPs synthesized through ECD methods are electron-richer than those of PdNPs/CeO₂-IM catalysts. The O 1s XPS spectra of two samples exhibits a main peak at around 529 eV and a shoulder peak at about 531 eV. The main peak at around 529 eV can be assigned to lattice oxygen of bulk CeO₂, and the shoulder peak at about 531 eV represents surface chemisorbed oxygen [28]. The more surface chemisorbed oxygen for PdNPs/CeO₂-ECD is ascribed to a higher portion of surface oxygen vacancies which can contribute to the activation of O₂ and accelerate the reaction rate of CO oxidation. Thus, the strong electronic metal–support interaction (EMSI) is evidenced in PdNPs/CeO₂-ECD.
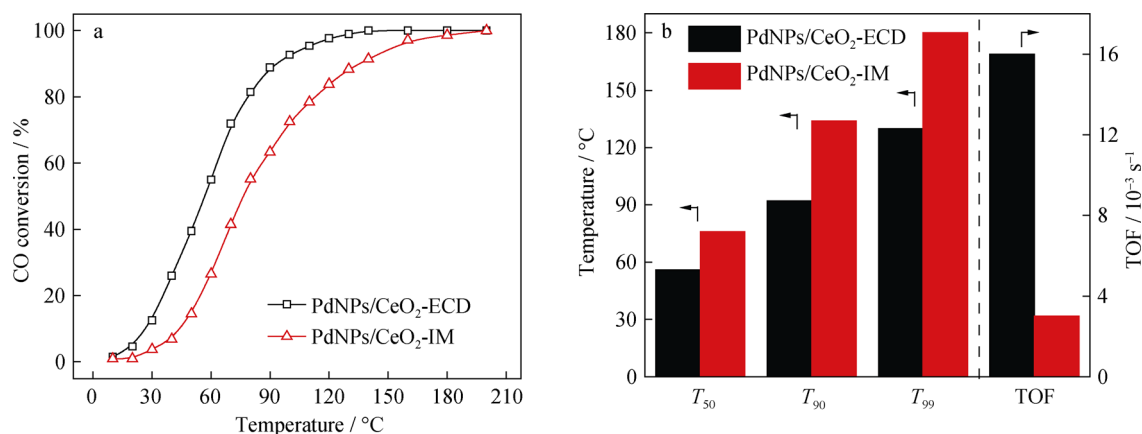
Fig. 5 **a** Catalytic performance for CO oxidation and **b** comparison of T_{50}, T_{90}, T_{99} and corresponding Turnover frequency (TOF) values of PdNPs/CeO$_2$-ECD and PdNPs/CeO$_2$-IM at 30 °C, respectively
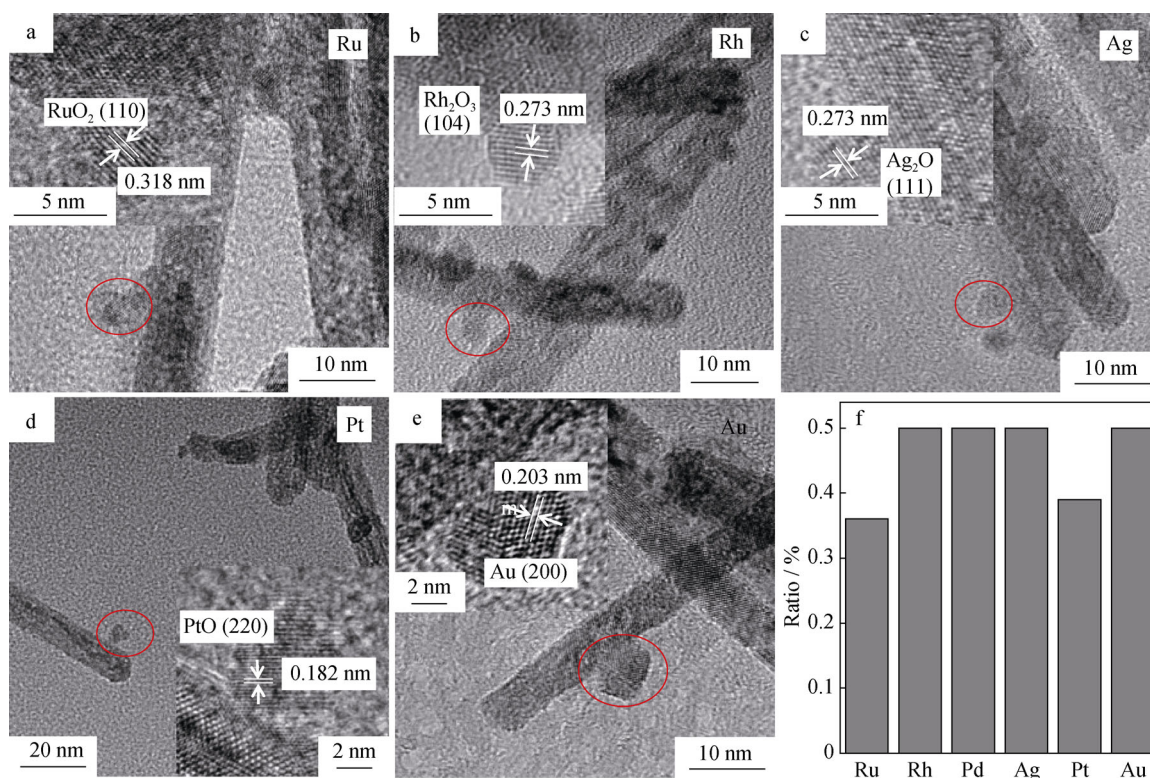

Fig. 6 Typical TEM and HRTEM images of different **a** Ru, **b** Rh, **c** Ag, **d** Pt and **e** Au nanoparticles planted on CeO$_2$ nanorods synthesized via ECD method; **f** actual loading amounts of noble metals (with theoretical value of 0.5 wt%) determined by ICP-AES

3.5 CO oxidation test

Noble metals (Pd, Pt, Au, Ag, etc.) anchored on various supports are broadly explored for CO oxidation in automobile exhaust catalytic reactions, water–gas shift reaction and preferential oxidation of CO in excess hydrogen [29–34]. Herein, CO oxidation was designated as a model reaction to evaluate the catalytic activity of the PdNPs/CeO$_2$ synthesized by ECD and impregnation methods. As

revealed in the light-off curves (Fig. 5a), the PdNPs/CeO$_2$-ECD catalysts delivered the much better catalytic activity for CO oxidation than the PdNPs/CeO$_2$-IM catalysts. As presented in Fig. S10 and Fig. 5b, the corresponding Arrhenius plots revealed that the apparent activation energy (E_a) of the PdNPs/CeO$_2$-ECD catalysts was 36.9 kJ·mol^{-1}, smaller than the value of 53.4 kJ·mol^{-1} for the PdNPs/CeO$_2$-IM catalysts. Derived from light-off curves, as exhibited in Fig. 5b, T_{50}, T_{90} and T_{99} at the

temperatures of 50%, 90% and 99% CO conversions for the PdNPs/CeO$_2$-ECD catalysts were also much smaller than those for the PdNPs/CeO$_2$-IM catalysts. For example, T_{99} for PdNPs/CeO$_2$-ECD catalysts was 130 °C, which was 53 °C lower than the corresponding value of 183 °C for PdNPs/CeO$_2$-IM catalysts. Furthermore, turnover frequency was calculated to compare their intrinsic catalytic activity at 30 °C (CO conversion < 20%), indicating a higher intrinsic catalytic activity of PdNPs/CeO$_2$-ECD, compared to PdNPs/CeO$_2$-IM (Fig. 5b). Pd/CeO$_2$ catalyst with 2% loading synthesized through the thermal decomposition method completely transformed CO to CO$_2$ over 150 °C [35]. The catalytic activity of Pd/CeO$_2$ catalyst prepared by co-precipitation method is also much lower than that of PdNPs/CeO$_2$-ECD in this work [36]. Therefore, ECD method is a facile and simple way to prepare highly efficient catalysts.

Although PdNPs/CeO$_2$-IM exhibits a higher dispersion of Pd nanoparticles, their catalytic activity was much lower than that of PdNPs/CeO$_2$-ECD. First of all, the in situ growth of Pd nanoparticles on CeO$_2$ by ECD method delivers uniform particles and prominent EMSI effect with enhanced reducibility and anti-sintering capability at high temperatures, which facilitate higher catalytic activity of PdNPs/CeO$_2$-ECD for CO oxidation. Secondly, surface electron enrichment on Pd induced by EMSI can modulate the CO absorption on the metal surface and inhibit CO poison effect [17]. Also, the abundant surface oxygen vacancies improve oxygen activation. Thirdly, it has been proofed by previous literatures that the existence of chloride ions can poison the noble metal catalysts and restrain the activity of catalysts subsequently [37, 38]. The presence of chloride ions also can fill the oxygen vacancies close to the interfaces of Pd nanoparticles and ceria and further depress the spillover and back-spillover speed of reactants seriously [38]. XPS profiles (Fig. S11) indicate the existence of chlorine in PdNPs/CeO$_2$-IM. The residual chloride ions in PdNPs/CeO$_2$-IM are deleterious to the catalytic activity of Pd active components. In contrast, chlorine is barely detectable in PdNPs/CeO$_2$-ECD. Therefore, the high catalytic activity of Pd/CeO$_2$-ECD catalysts can be ascribed to the combination of the uniform Pd nanoparticles, stronger electronic metal–support interaction and clean surface-active sites given by ECD method, which makes ECD technique practical for synthesis of nanoscaled catalysts.

3.6 General synthesis of metal/CeO$_2$

The current ECD method can be further extended to plant series of noble metal particles on CeO$_2$ supports. Successful deposition of uniform noble metal catalysts (e.g., Ru, Rh, Ag, Pt and Au) was realized through the similar synthetic process between the reduced CeO$_2$ nanorods and noble metal precursors. Typical TEM and HRTEM images and size distributions are presented in Fig. 6a–e and Fig. S12, showing the small size (< 3 nm) of noble metal particles. Figure 6f shows the actual loadings of noble metals on CeO$_2$ nanorods, where the theoretical value was fixed at 0.5 wt% for all noble metals. The metal loadings of Rh, Ag and Au were completely planted on CeO$_2$ nanorods, while the metal loadings of Ru and Pt were smaller than 0.5 wt%. Therefore, successful realization of decoration of various noble metal nanoparticles on CeO$_2$ further proves that this ECD technique is a facile, effective and universal approach to synthesize small nanoparticles on CeO$_2$ supports.

4 Conclusion

In summary, we develop a feasible, scalable and universal ECD technique as a facile and green synthetic approach to plant uniform and small Pd nanoparticles ($\sim$ 2.5 nm) as well as other noble metals (Ru, Rh, Ag, Pt and Au) on the reducible CeO$_2$ nanorod supports under ambient conditions. This method with high repeatability is cost-effective, efficient and time-saving. Moreover, the absence or decreased usage of surfactants and other chemicals can reduce the fabrication cost, possibility in the secondary environmental contamination and poison on the catalytic sites. Specifically, the PdNPs/CeO$_2$-ECD catalysts deliver a higher activity for CO oxidation due to their uniform Pd catalysts, chlorine-free, stronger metal–support interaction associated with high reducibility and strong anti-sintering capability, compared to the catalysts prepared by impregnation method. We believe the developed ECD method in this work delivers well-defined heterogeneous composites, which have great potential applications in catalysis as well as numerous other frontiers.

References

[1] Barakat T, Rooke JC, Genty E, Cousin R, Siffert S, Su BL. Gold catalysts in environmental remediation and water–gas shift technologies. Energy Environ Sci. 2013;6(2):371.

[2] Liu LC, Corma A. Metal catalysts for heterogeneous catalysis: from single atoms to nanoclusters and nanoparticles. Chem Rev. 2018;118(10):4981.

[3] Ma YY, Gao W, Zhang ZY, Zhang S, Tian ZM, Liu YX, Ho JC, Qu YQ. Regulating the surface of nanoceria and its applications in heterogeneous catalysis. Surf Sci Rep. 2018;73(1):1.

[4] Ahmadi M, Mistry H, Cuenya BR. Tailoring the catalytic properties of metal nanoparticles via support interactions. J Phys Chem Lett. 2016;7(17):3519.

[5] Das J, Cederquist KB, Zaragoza AA, Lee PE, Sargent EH, Kelley SO. An ultrasensitive universal detector based on neutralizer displacement. Nat Chem. 2012;4(8):642.

[6] Bruix A, Rodriguez JA, Ramirez PJ, Senanayake SD, Evans J, Park JB, Stacchiola D, Liu P, Hrbek J, Illas F. A new type of strong metal-support interaction and the production of H_2 through the transformation of water on $Pt/CeO_2(111)$ and $Pt/CeO_x/TiO_2(110)$ catalysts. J Am Chem Soc. 2012;134(21):8968.

[7] Tang H, Su Y, Zhang B, Lee AF, Isaacs MA, Wilson K, Li L, Ren YG, Huang JH, Haruta M, Qiao BT, Liu X, Jin CZ, Su DS, Wang JH, Zhang T. Classical strong metal–support interactions between gold nanoparticles and titanium dioxide. Sci Adv. 2017;3(10):e170023.

[8] Ro I, Resasco J, Christopher D. Approaches for understanding and controlling interfacial effects in oxide-supported metal catalysts. ACS Catal. 2018;8(8):7368.

[9] Matsubu JC, Zhang SY, Derita L, Marinkovic Chen JG, Graham GW, Pan XQ, Christopher P. Adsorbate-mediated strong metal-support interactions in oxide-supported Rh catalysts. Nat Chem. 2017;9(2):120.

[10] Hou TT, Wang YH, Zhang J, Li MR, Lu JM, Heggen M, Sievers C, Wang F. Peculiar hydrogenation reactivity of $Ni-Ni^{\sigma+}$ clusters stabilized by ceria in reducing nitrobenzene to azoxybenzene. J Catal. 2017;353:107.

[11] Wang M, Wang F, Ma JP, Li MR, Zhang Z, Wang YH, Zhang XC, Xu J. Investigations on the crystal plane effect of ceria on gold catalysis in the oxidative dehydrogenation of alcohols and amines in the liquid phase. Chem Commun. 2014;50(3):292.

[12] Acerbi N, Tsang S, Jones G, Golunski S, Collier P. Rationalization of interactions in precious metal/ceria catalysts using the d-band center model. Angew Chem Int Ed. 2013;52(30):7737.

[13] Munnik P, Jongh P, Jong K. Recent developments in the synthesis of supported catalysts. Chem Rev. 2015;115(14):6687.

[14] Guo Y, Mei S, Yuan K, Wang DJ, Liu HC, Yan CH, Zhang YW. Low-temperature CO_2 methanation over CeO_2-supported Ru single atoms, nanoclusters, and nanoparticles competitively tuned by strong metal-supported interactions and H-spillover effect. ACS Catal. 2018;8(7):6203.

[15] Wang WW, Yu WZ, Du PP, Xu H, Jin Z, Si R, Ma C, Shi S, Jia CJ, Yan CH. Crystal plane effect of ceria on supported copper oxide cluster catalysts for CO oxidation: importance of metal-supported interaction. ACS Catal. 2017;7(2):1313.

[16] Liu K, Wang AQ, Zhang T. Recent advances in preferential oxidation of CO reaction over platinum group metal catalysts. ACS Catal. 2012;2(6):1165.

[17] Cao FX, Zhang S, Gao W, Cao T, Qu YQ. Facile synthesis of highly-dispersed Pt/CeO_2 by a spontaneous surface redox chemical reaction for CO oxidation. Catal Sci Technol. 2018;8(13):3233.

[18] Xi GC, Ye JH, Ma Q, Su N, Bai H, Wang C. In situ growth of metal particles on 3D urchin-like WO_3 nanostructures. J Am Chem Soc. 2012;134(15):6508.

[19] Xie Y, Ding KL, Liu ZM, Tao RT, Sun ZY, Zhang HY, An GM. In situ controllable loading of ultrafine noble metal particles on titania. J Am Chem Soc. 2009;131(19):6648.

[20] Mitsudome T, Yamamoto M, Maeno Z, Mizugaki T, Jitsukawa K, Kaneda K. One-step synthesis of core-gold/shell-ceria nanomaterial and its catalysis for highly selective semihydrogenation of alkynes. J Am Chem Soc. 2015;137(42):13452.

[21] Bensalem A, Shafeev G, Bozon-Verduraz F. Application of electroless procedures to the preparation of palladium catalysts. Catal Lett. 1993;18(1–2):165.

[22] Li J, Zhang ZY, Tian ZM, Zhou XM, Zheng ZP, Ma YY, Qu YQ. Low pressure induced porous nanorods of ceria with high reducibility and large oxygen storage capacity: synthesis an catalytic applications. J Mater Chem A. 2014;2(39):16459.

[23] Mai HX, Sun LD, Zhang YW, Si R, Feng W, Zhang HP, Liu HC, Yan CH. Shape-selective synthesis and oxygen storage behavior of ceria nanopolyhedra, nanorods, and nanocubes. J Phys Chem B. 2005;109(51):24380.

[24] Tang XL, Zhang BC, Li Y, Xu YD, Xin Q, Shen WJ. Structural features and catalytic properties of Pt/CeO_2 catalysts prepared by modified reduction-deposition techniques. Catal Lett. 2004;97(3–4):163.

[25] Wei YC, Liu J, Zhao Z, Duan AJ, Jiang GY. The catalysts of three-dimensionally ordered macroporous $Ce_{1-x}Zr_xO_2$-supported gold nanoparticles for soot combustion: the metal-support interaction. J Catal. 2012;287:13.

[26] Xu LL, Pu CH, Wang L, Guo Y, Guo YL, Lu GZ. Effect of calcination temperature on meso-$Pd/Fe(OH)_x$ for CO oxidation at low temperature. Chin J Rare Met. 2018;42(2):161.

[27] Qu J, Zhou XW, Xu F, Gong XQ, Tsang S. Shape effect of Pd-promoted Ga_2O_3 nanocatalysts for methanol synthesis by CO_2 hydrogenation. J Phys Chem C. 2014;118(42):24452.

[28] Tan HY, Wang J, Yu SZ, Zhou KB. Support morphology-dependent catalytic activity of Pd/CeO_2 for formaldehyde oxidation. Environ Sci Technol. 2015;49(14):8675.

[29] Zhang SR, Shan JJ, Zhu Y, Nguyen L, Huang WX, Yoshida H, Takeda S, Tao FF. Restructuring transition metal oxide nanorods for 100% selective in reduction of nitric oxide with carbon monoxide. Nano Lett. 2013;13(7):3310.

[30] Rodriguez JA, Grinter DC, Liu ZY, Polomino RM, Senanayake SD. Ceria-based model catalysts: fundamental studies on the importance of the metal-ceria interface in CO oxidation, the water–gas shift, CO_2 hydrogenation, and methane and alcohol reforming. Chem Soc Rev. 2017;46(7):1824.

[31] Wen C, Zhu Y, Ye YC, Zhang SR, Cheng F, Liu Y, Wang P, Tao FF. Water-gas shift reaction on metal nanoclusters encapsulated in mesoporous ceria studied with ambient-pressure X-ray photoelectron spectroscopy. ACS Nano. 2012;6(10):9305.

[32] Tao FF, Ma Z. Water-gas shift on gold catalysts: catalysts systems and fundamental studies. Phys Chem Chem Phys. 2013;15(37):15260.

[33] Du PP, Wang WW, Jia CJ, Song QS, Huang YY, Si R. Effect of strongly bound copper species in copper-ceria catalyst for preferential of carbon monoxide. Appl Catal A Gen. 2016;518:87.

[34] Chen YS, Cao YD, Ran R, Wu XD, Weng D. Controlled pore size of Pt/KIT-6 used for propane total oxidation. Rare Met. 2018;37(2):123.

[35] Gulyaev RV, Stadnichenko AI, Slavinskaya EM, Ivanova AS, Koscheev SV, Boronin AI. In situ preparation and investigation of Pd/CeO_2 catalysts for the low-temperature oxidation of CO. Appl Catal A Gen. 2012;439:41.

[36] Slavinskaya EM, Gulyaeva RV, Zadesenets AV, Stonkus OA, Zaikovskii VI, Shubinb YV, Korenev SV, Boronin AI. Low-temperature CO oxidation by Pd/CeO_2 catalysts synthesized using the coprecipitation method. Appl Catal B Environ. 2015;166:91.

[37] Kung MC, Davis RJ, Kung HH. Understanding Au-catalyzed low-temperature CO oxidation. J Phys Chem C. 2007;111(32):767.

[38] Gayen A, Boaro M, de Leitenburg C, Llorca J, Trovarelli A. Activity, durability and microstructural characterization of ex-nitrate and ex-chloride $Pt/Ce_{0.56}Zr_{0.44}O_2$ catalysts for low temperature water gas shift reaction. J Catal. 2010;270:285.